$Li_4Ru_2OCl_{10}$ •$10H_2O$: Crystal Structure, Magnetic Properties, and Bonding Interactions in Ruthenium-Oxo Complexes

Ranuri S Dissanayaka Mudiyanselage,[a] Madalynn Marshall,[a] Tai Kong,[b] Weiwei Xie[a*]

[a.] *Department of Chemistry, Louisiana State University, Baton Rouge, LA, 70803, USA*
[b.] *Department of Physics, University of Arizona, Tucson, AZ, 85721, USA*

Abstract

The results of the structural determination, magnetic characterization, and theoretical calculations of a new Ru oxo complex, $Li_4[Ru_2OCl_{10}]$ •$10H_2O$, are presented. Single crystals were grown using solvent methods, and the crystal structure was characterized by single crystal X-ray diffraction. $Li_4[Ru_2OCl_{10}]$ •$10H_2O$ crystallizes into a low symmetry triclinic structure (S.G. *P*-1) due to the much smaller Li^+ compared to K^+ in the tetragonal $K_4[Ru_2OCl_{10}]$ •H_2O. The X-ray photoelectron spectra confirms only the single valent Ru^{4+} in $Li_4[Ru_2OCl_{10}]$ •$10H_2O$ even though two distinct Ru sites exist in the crystal structure. Magnetic measurements reveal the diamagnetic property of $Li_4[Ru_2OCl_{10}]$ •$10H_2O$ with unpaired electrons existing on Ru^{4+}. Furthermore, the molecular orbital analysis matches well with the observed UV and magnetic measurements.

1 Introduction

The material community constantly explores the limits and boundaries of existing compounds to understand their structural stabilities and functional behaviors, which provides a platform for designing novel materials with better optimized properties (Butler *et al.*, 2018; Zhuo *et al.*, 2018; Curtarolo *et al.*, 2013; Rivero *et al.*, 2017) The Ruddlesden-Popper perovskite family $Sr_{(n+1)}Ru_nO_{(3n+1)}$ (n = 1,2,3,….) is a characteristic example that has demonstrated interesting properties ranging from superconductivity (Maeno *et al.*, 1994), metallic ferromagnetism (Fobes *et al.*, 2007) to antiferromagnetic conductors (Huang *et al.*, 1998). Among them, $Sr_3Ru_2O_7$ containing two layers of RuO_6 octahedra connected by an apical oxygen atom is a paramagnetic metal in its ground state (Ikeda & Maeno, 1999). The two RuO_6 octahedra exhibit a unique twisting formation in $Sr_3Ru_2O_7$, where one RuO_6 is rotated clockwise by 8.05° and the other is rotated counter-clockwise by the same degree (Rivero *et al.*, 2017) about the connecting oxygen atom. Due to this unique structural feature, defects can occur within the structure and lead to different electronic and magnetic properties with applied external parameters such as temperature (Stone *et al.*, 2006), composition (Steffens *et al.*, 2009) and magnetic field (Perry *et al.*, 2000; Grigera *et al.*, 2003). Recently, the 4*d*/5*d*-based compounds with a strong spin-orbit coupling (SOC) effect has attracted a lot of attention because their electronic ground state can generate various unconventional physical phenomena such as quantum spin liquids (QSL), axion insulators, and so on (Zhou *et al.*, 2017; Li *et al.*, 2010; Pesin & Balents, 2010). Most experimental and theoretical studies focus on d^5 systems with S=1/2, for example, a-$RuCl_3$ (Okamoto *et al.*, 2007; Banerjee *et al.*, 2016). The resulting magnetic moments originate from the unpaired electrons in the *d*-orbitals of the transition metals in these magnetic insulating solids (Coey, 2010). For some of them, magnetic interactions will not order even at low temperatures due to the frustrated lattice geometry (Nakatsuji *et al.*, 2006). An outstanding example of magnetic frustration is the Kitaev model in the honeycomb lattice, which forms a quantum spin liquid state (Banerjee *et al.*, 2016; Kitaev, 2006). Geometric magnetic frustration is well-observed in solids with triangular geometry. $Ba_4NbRu_3O_{12}$, with its magnetic moment originating in the Ru_3O_{12} trimers, has attracted a lot of attention in exploring QSL materials with novel geometric frustrations (Nguyen *et al.*, 2018). The Ru_3O_{12} trimers in $Ba_4NbRu_3O_{12}$ and the RuO_6 dimers in $Sr_3Ru_2O_7$ inspired us to investigate the magnetic properties of magnetic molecules consisting of transition metal oxo complexes for example, ruthenium-oxo complexes (Ru-O-Ru).

The importance of molecule-based magnets has emerged with various potential applications, such as quantum computing. Generally, there are two families of molecule-based magnets. One is the single-molecule magnet (SMM), which hosts superparamagnetic behaviors below a certain blocking temperature at the molecular scale (Guo *et al.*, 2018). The other is the conventional molecule-based magnet, which is typically associated with properties such as transparency, electrical insulation, and even photo-responsiveness.

The di-metallic molecular clusters bridged by oxo, hydroxo or even water molecules are usually classified into conventional molecule-based magnets. Such materials are interesting due to their structural simplicity for studying the exchange pathway in magnetochemistry without the inherent complications coming from different ions simultaneously in multinuclear compounds (Overgaard *et al.*, 2014; Walsh *et al.*, 2014; Gorun & Lippard, 1991). Most oxo-di-metallic molecular clusters have been well studied for their catalytic properties and medicinal applications (Zimmermann *et al.*, 2018; Arii *et al.*, 2000; Kurtz, 1990; Engelmann *et al.*, 2016). However, limited research has been conducted to understand their magnetic properties (Sessoli *et al.*, 1993; Singh & Rajaraman, 2019; Lang *et al.*, 2018; Barman *et al.*, 2019). Even though solid conclusions on magneto-structural correlations are skeptical and largely differ from system to system, up to date studies reveal that the bridging bond angle is a crucial parameter in this context. The bridging angle is corelated with the sign of the magnetic exchange interaction (Boeer *et al.*, 2011; Crawford *et al.*, 1976) and has been used to support the hypothesis of the super exchange pathways occurring, for example, via the bridging water molecule in dinickel carboxylate complexes (Walsh *et al.*, 2014). In addition, it suggests that smaller M-O-M angles give rise to ferromagnetic (FM) interactions while larger angles give rise to antiferromagnetic (AFM) interactions (Walsh *et al.*, 2014). Furthermore, a recent study has shown that with a slight variation in chemical composition and structure in a class of water bridged dimer compounds, contrasting exchange interactions of AFM or FM exists, which was discovered without a clear understanding for the reason behind this behavior (Boeer *et al.*, 2011). The other common correlation parameter of the metal to bridge bond distance has been well established by Gorun and Lippard(Gorun & Lippard, 1991) using 36 di-nuclear complexes that has been further confirmed by later studies as well (Halcrow *et al.*, 1995).

With this motivation in mind, we focus on studying the magnetic interactions in a ruthenium oxo dimer molecule moving away from the complexity in the crystalline solids with the Ru-O-Ru octahedral units. The previously reported complexes in the family of $A_4[Ru_2OCl_{10}]$ (A= K and Cs) possess a linear Ru-O-Ru bond rather than a twisted octahedra geometry. The question is whether a new compound from the same family can host any possible twisted octahedra as observed in $Sr_3Ru_2O_7$. Herein, we used the smaller cation Li^+ to replace K^+ and Cs^+. As a result, a lithium counterpart and novel di-metallic ruthenium complex, $Li_4[Ru_2OCl_{10}]\bullet 10H_2O$, was discovered. The structure and magnetic properties were characterized with a combination of experimental and theoretical assessments to clarify the intrinsic interplay of electrons and spin.

2 Experimental Parts

2.1 Synthesis:

The purchased $RuCl_3 \cdot nH_2O$ (Emsure, Sigma Aldrich, powder) was dried in an oven at 110°C for 12 hours. 5 mmol (1.0426 g) was weighed immediately after being removed from the oven and dissolved in 25 ml absolute ethanol (Emsure, Sigma Aldrich) to make Solution 1. The Solution 2 was prepared by mixing 35 mmol (1.5010 g) of anhydrous LiCl (99%, Alfa Aesar, crystals), 30 mmol (3.5420 g) of succinic acid (99+%, Alfa Aesar, crystals), 6 mmol (0.6032 g) of succinic anhydride (99%, Alfa Aesar, crystalline flakes) in 75 ml of absolute ethanol. The Solution 2 was added to the round bottom flask containing Solution 1 and refluxed at 70 ^{o}C for 3.5 hours in the stream of oxygen gas. The resulting dark brown solution was cooled to room temperature naturally and gravity filtered. The mother solution was placed in a loosely capped vial for about two weeks at room temperature to obtain the crystals. The brown colored crystals obtained were unstable in air outside of the mother solution. Therefore, the crystals were separated by removing the mother solution in an argon filled glovebox and dried in a vacuum for further studies.

2.2 Structure Determination:

Several crystals were picked from the mother solution, protected by glycerol, and mounted on a Kapton loop. The measurements were conducted at 90(2) K with the liquid N_2 protection in a Bruker Apex II diffractometer with Mo radiation ($\lambda_{K\alpha}$ = 0.71073 Å). The exposure time and scanning 2θ width were set up as 10 s and 0.5° per frame, respectively. Direct method and full matrix least-squares on F^2 model with the SHELXTL was used for the structure solving and refinement. The structure was refined with anisotropic thermal parameters for all non-hydrogen atoms in SHELXTL. Hydrogen attached to the considered oxygen atoms were determined geometrically using the peaks in the difference map and refined with fixed thermal parameter of $U_{iso}(H)=1.2U_{eq}(O)$ (Sheldrick, 2015; Mousavi *et al.*, 2012; Bai *et al.*, 2004; Lu *et al.*, 2018)

2.3 X-ray photoelectron spectra (XPS) Measurements:

The X-ray photoelectron spectra was collected on crystals with a base pressure of 3.8×10^{-9} mbar. The Scienta Omicron ESCA 2SR spectroscope was used with a mono Al anode of 15 kV and 300 W. The analysis area is around 3 mm. The crystalline sample was mounted on carbon tape. Data analysis including calibration, deconvolution, and quantification was done using the Casa XPS software.

2.4 Physical Property Measurements:

Magnetic properties were measured using a DynaCool physical property measurement system (PPMS) on a collection of samples, with a total mass of 10.9 mg, packed in an argon filled glovebox. The instrument was operated over a temperature range of 1.8-300 K and an applied field up to 90 kOe.

2.5 Generation of the Molecular Orbital (MO) Diagram of $Li_4Ru_2OCl_{10}$•$10H_2O$

The molecular orbital diagram was generated using CEASER software with the extended Huckel method (Hoffmann, 1963; Naito et al., 2019; Gui et al., 2019). The parameters set used in the calculation is given in the **Table 1**.

3 Results and Discussion

3.1 Crystal Structure of $Li_4Ru_2OCl_{10}$ •$10H_2O$:

The crystal structure of the brown transparent single crystals obtained from the slow evaporation of the solvent was determined using a single-crystal X-Ray diffractometer at 90 K under liquid N_2 protection. The results of the single-crystal X-ray diffraction (SCXRD) study including refinement details, atomic positions, site occupancies, and isotropic thermal displacements for all non-hydrogen atoms are summarized in **Tables 2 and 3**. Structural information regarding the hydrogen atoms is summarized in **Table S1**. The anisotropic thermal displacements are provided in **Table S2**.

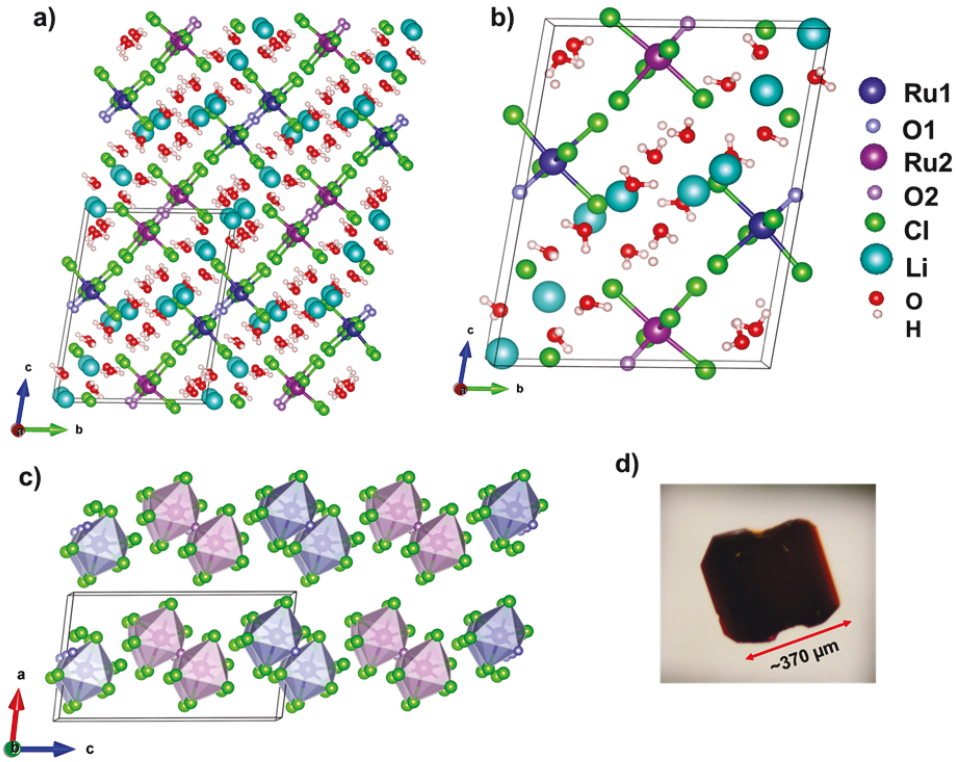

Figure 1

Crystal structure of $Li_4Ru_2OCl_{10}$•$10H_2O$ showing the arrangement of the lattice in the *a*). *bc* plane showing the dimeric anion $[Ru_2OCl_{10}]^{4-}$ and Li^+ cations network; *b*). Atomic distribution in one-unit cell; *c*). Two $[Ru_2OCl_{10}]^{4-}$ anions showing vertex shared octahedra in the *ac* plane. *d*). The crystal image of $Li_4Ru_2OCl_{10}$•$10H_2O$.

According to the SCXRD results, the compound adopts a triclinic structure with space group *P*-1 (No. 2). The $Li_4Ru_2OCl_{10}$•$10H_2O$ molecular structure consists of ruthenium complex anion $[Ru_2OCl_{10}]^{4-}$ layers with an intercalated H_2O coordinated Li^+ cation network as shown in **Figure 1*a***. Each unit cell is filled up with eight Li, four Ru, two O, and 20 Cl atoms as well as 20 H_2O molecules as shown in **Figure 1*b***. Four Ru atoms occupy two

151 distinct Ru sites. Thus, the two distinct $[Ru_2OCl_{10}]^{4-}$ anions per unit cell are the key structural
152 feature governing the magnetic properties in this compound, as depicted in **Figure 1*c***. The
153 anion $[Ru_2OCl_{10}]^{4-}$ is a vertex sharing octahedra *via* O atoms and shows a layered
154 arrangement extending to 3-dimensional space. The two $[Ru_2OCl_{10}]^{4-}$ anions are in contrast to
155 other reported $A_4[Ru_2OCl_{10}]$ compounds, which have only one Ru site in the crystal structure
156 (McL Mathieson *et al.*, 1952; Silva *et al.*, 1999; Tebbe & Schnering, 1973; Glowiak *et al.*).
157 Each $[Ru_2OCl_{10}]^{4-}$ complex is formed by two identical Ru atoms linked *via* an O-bridge
158 leading to an inversion symmetry within the anion. Each Ru atom connects with five terminal
159 Cl atoms and a bridging O atom, which results in a dimer with the neighboring Ru atom. The
160 Ru-Cl bonding distances range from 2.3406(4) Å to 2.3646(5) Å for Ru1-Cl, and 2.3358(4) Å
161 to 2.3922(4) Å for Ru2-Cl, respectively. The Ru1-O and Ru2-O distances are 1.7838(3) Å
162 and 1.7808(3) Å. This indicates that the distortion of the Ru2 anion complex is comparatively
163 higher than for Ru1.

164 $Li_4Ru_2OCl_{10}\bullet 10H_2O$ crystalizes into a lower symmetry space group (*P*-1) compared
165 to its family compounds, $K_4Ru_2OCl_{10}\bullet H_2O$ (*I*4/*mmm*) (McL Mathieson *et al.*, 1952; San
166 Filippo *et al.*, 1977), $Cs_4Ru_2OCl_{10}$ (*Pbca*) (San Filippo *et al.*, 1977; Silva *et al.*, 1999),
167 $K_4W_2OCl_{10}$ (*I*4/*mmm*) (Glowiak *et al.*) and $Cs_4Os_2OCl_{10}$ (*Pcab*) (Tebbe & Schnering, 1973).
168 The compounds share the common bi-nuclear $[Cl_5M\text{-}O\text{-}MCl_5]^{4-}$ (M= Ru, Os) anions with
169 different degrees of distortions within the dioctahedral (McL Mathieson *et al.*, 1952; Tebbe &
170 Schnering, 1973; Glowiak *et al.*). The size of the cations is critical to induce the structural
171 distortion in $Li_4Ru_2OCl_{10}\bullet 10H_2O$. More specifically, the bi-nuclear moiety in
172 $K_4Ru_2OCl_{10}\bullet H_2O$ is sharing an exact D_{4h} symmetry with Ru, O and Cl_{ax} atoms on the 4-fold
173 axis while $Cs_4Ru_2OCl_{10}$ possesses a slightly distorted unit from tetragonal to orthorhombic,
174 compared to $K_4Ru_2OCl_{10}\bullet H_2O$ (Silva *et al.*, 1999). Furthermore, the same fragment in
175 $Li_4Ru_2OCl_{10}\bullet 10H_2O$ shows a significant distortion compared to $K_4Ru_2OCl_{10}\bullet H_2O$ and
176 $Cs_4Ru_2OCl_{10}$ referring to the bond angles and bond lengths given in **Table 4**. In the Ru1
177 dimer, the Ru-Cl_{eq} bond length has a difference of ~0.008 Å while in the Ru2 dimer, this
178 value is ~0.05 Å that is about ten times larger than the 0.004 Å bond length difference in the
179 $Cs_4Ru_2OCl_{10}$ Ru2 dimer. Therefore, with the substitution of the smaller Li cation in
180 $A_4Ru_2OCl_{10}$, the binuclear anion complex has been distorted considerably. Despite the overall
181 distortion of the anion complex, the Ru-O-Ru unit is perfectly linear as observed in other
182 compounds (McL Mathieson *et al.*, 1952; Silva *et al.*, 1999; Tebbe & Schnering, 1973;
183 Glowiak *et al.*). However, a closer look at this structure shows that the adjacent $[Ru_2OCl_{10}]^{4-}$

fragments are layered off set to each other and two dimers are arranged alternatively in the anion layers as shown in the **Figure 1*c***, which likely occur to further enhance the crystal packing. Moreover, the cation network has intercalated between these layers of anion. The four Li^+ cations are surrounded by the ten water molecules in the structure, which is in contrast to the previously reported $A_4[Ru_2OCl_{10}]$ compounds (McL Mathieson *et al.*, 1952; Silva *et al.*, 1999). The fact that $Li_4Ru_2OCl_{10}$•$10H_2O$ is composed of more water molecules in its structure than in compounds with larger cations K^+(151pm) (Rollinson & Adetunji, 2018) and Cs^+(174pm) (Rollinson & Adetunji, 2018), can be explained as a way to compensate for the empty space around the much smaller Li^+ (~59-76pm) (Rollinson & Adetunji, 2018) cation and thus stabilize the crystal structure. However, each Li+ ion coordinates differently, which has also been observed in $Cs_4Ru_2OCl_{10}$ and $Cs_4Os_2OCl_{10}$ (Silva *et al.*, 1999; Tebbe & Schnering, 1973).

Overall, by solely looking at the refined formula for the compound, the two Ru atoms can have either a +4 oxidation state or mixed oxidation states of +3 and +5 on each Ru atom. However, the nearly equal Ru-O bond lengths indicates a similar oxidation state in both Ru atoms rather than a mixed oxidation state (Sharninghausen *et al.*, 2016).

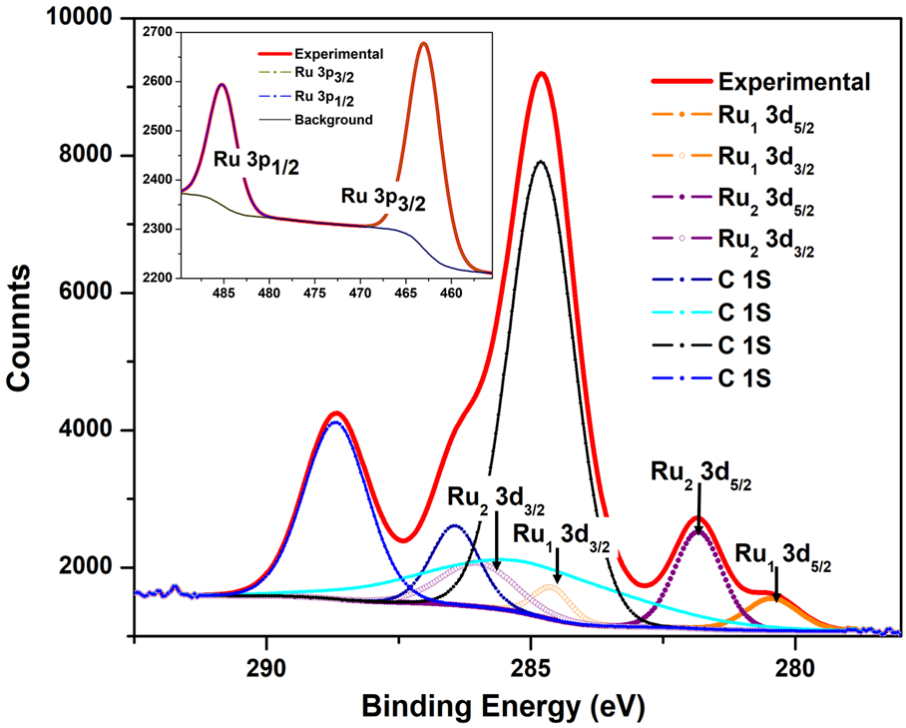

Figure 2

XPS spectrum of $Li_4Ru_2OCl_{10}$•$10H_2O$ with its simulated peak fitting of Ru 3*d* (Inset: Ru 3*p* fitting).

3.2 Oxidation States of Ru in $Li_4Ru_2OCl_{10}$ •$10H_2O$:

X-ray photoelectron spectroscopic (XPS) measurements, shown in **Figure 2**, were carried out to determine the chemical oxidation states of Ru atoms in $Li_4Ru_2OCl_{10}$•$10H_2O$. The binding energies of the Ru 3*d* level highly overlap with the C 1*s* region which makes the interpretation of the Ru 3*d* region difficult and as a result the Ru 3*p* level has been used for a better understanding (Bo *et al.*, 2015; Costa *et al.*, 2011). According to the spectra of the Ru 3*d* region, binding energy values are in the range of Ru^{3+}/Ru^{4+} species. Even though, the overlapped signals make the interpretation complicated, it shows two possible Ru species with binding energies of 280.44 and 281.83 eV (Ru $3d_{5/2}$), and 284.61 and 286.00 eV (Ru $3d_{3/2}$). The peak at 280.44 eV (Ru $3d_{5/2}$) can be assigned to Ru^{4+} according to the previously reported data for Ru^{4+} at 281.37±1.32 eV (Morgan, 2015). This can be further confirmed by referring to the Ru 3*p* spectrum in **Figure. 2** *Inset*, which shows a peak at 462.91 eV (Ru 3*p* 3/2) indicating a Ru^{4+} species (Morgan, 2015). However, the Ru 3*p* spectrum shows only one type of Ru ion. The potential second Ru species is from the $RuCl_3$ impurity that can be ascribed to 281.83 eV (Ru 3d 5/2), this is later confirmed by magnetic measurements (Morgan, 2015). There were two O 1*s* peaks observed in the spectrum (**Figure S1**) with binding energies 531.72 eV and 533.47 eV. The higher binding energy value of 533.47 eV in the O 1*s* region can be attributed to the oxygen from the water molecules (Mercier *et al.*, 2006). The lower energy peak at 531.72 eV can be assigned to the O contributing to the Ru-O-Ru component of the dimer (Basova *et al.*, 2014). The binding energy values for photoelectron peaks of Ru and O are summarized in **Table S4**.

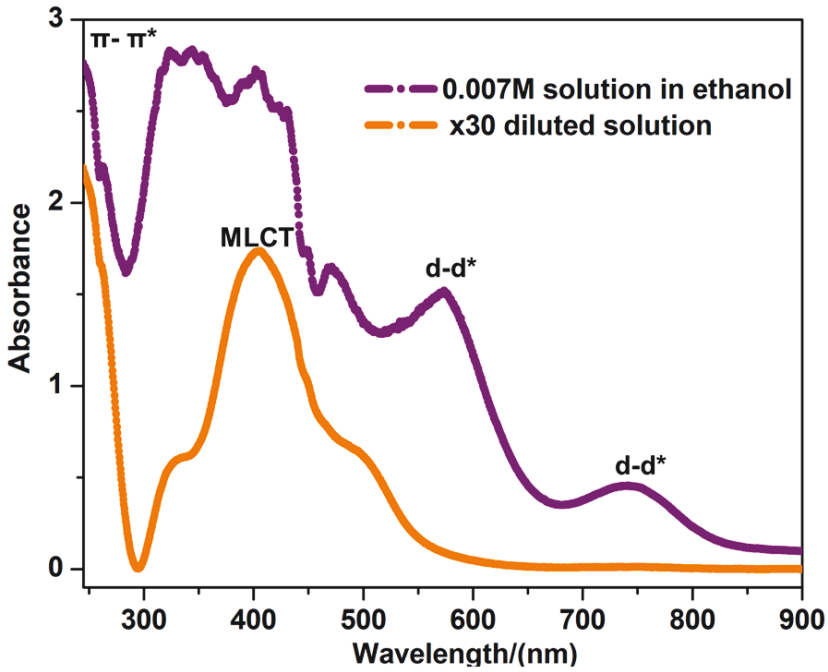

Figure 3

UV-Visible absorption spectra of $Li_4Ru_2OCl_{10}$•$10H_2O$.

3.3 UV-Visible Absorption Spectra of $Li_4Ru_2OCl_{10}$ •$10H_2O$:

The UV-Vis spectra of the complex were collected using absolute ethanol and the result is shown in **Figure 3**. According to the Beer Lambert law the absorption is directly proportional to the concentration of the solution. The concentration of the original sample is ~0.007 M. The concentrated solution of the compound shows two major peaks in the visible range at the wavelengths of 575 nm and 745 nm. The peak at 575nm is sharp and intense while the peak at 745 nm is broader and weaker in intensity. These two absorption peaks observed in the visible region can be assigned to the metal *d-d* transition - d_{xz}/d_{yz} to d_{xy} and to a higher energy orbital d_z^2 for 745 nm and 575 nm, respectively. In addition, the absorbance near the UV region is saturated at ~ 3.0 absorbance units with the concentration ~0.007 M. To obtain a clear spectrum in the UV region the same solution was diluted by 30 times. Upon dilution, the peaks observed from the visible region were diminished due to low absorbance, while the higher energy peaks close to the UV region became unsaturated and prominent. The high energy, high intensity peak arising with a maximum around 245 nm can be attributed to the π to π^* type transition of Ru-Cl. On the other hand, the absorption peak observed around 400 nm can be assigned to the metal to ligand charge transfer transitions (Maroń & Małecki, 2014; Ishiyama, 1969). The shoulder peak observed around 500 nm can be coming from Ru-O-Ru chromophore (San Filippo *et al.*, 1977). The shape and the wavelength of this peak is slightly different from the reported data for $K_4Ru_2OCl_{10}$, where a sharp narrow peak at 479 nm is observed. According to the electronic and vibrational spectra of $K_4Ru_2OCl_{10}$, the absorption at 479 nm, coming from the electronic transition, is coupled with the Ru-O-Ru symmetric stretching (San Filippo *et al.*, 1977). The shift to a lower energy absorption might be related to the structural symmetry difference between these two compounds. The $K_4Ru_2OCl_{10}$ structure is higher in symmetry (space group, *I*4/mmm) with a perfect D_{4h} symmetry in the dimer compared to our compound $Li_4Ru_2OCl_{10}$•$10H_2O$, which possesses a lower symmetry (space group, *P*-1) (McL Mathieson *et al.*, 1952).

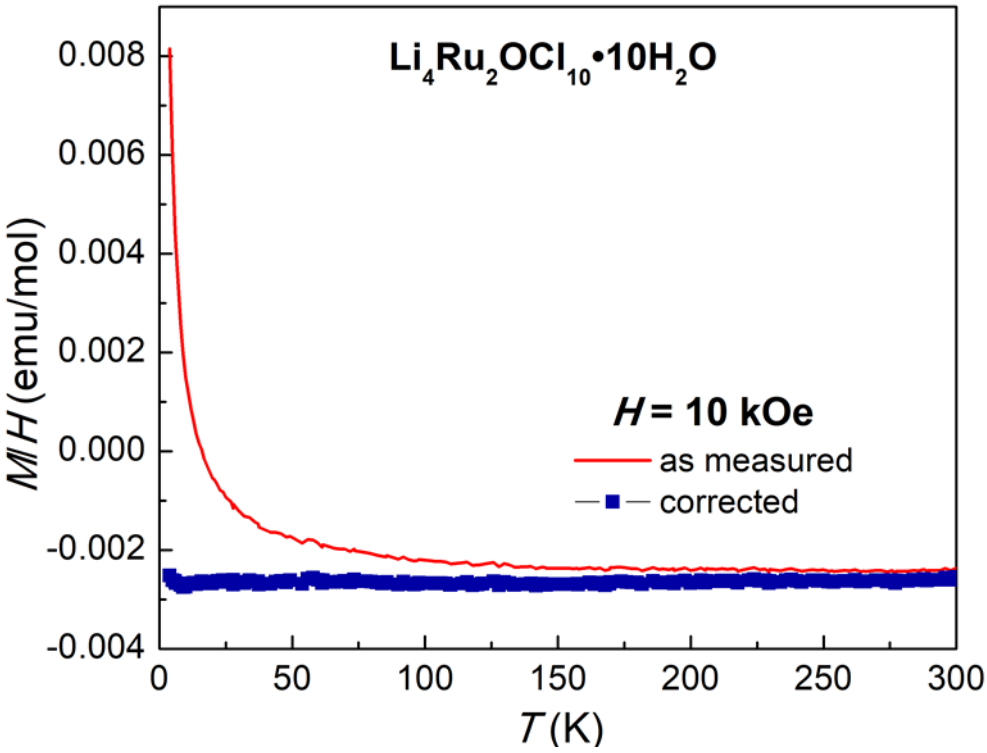

Figure 4

The temperature dependence of magnetic susceptibility measured at 10 kOe for $Li_4Ru_2OCl_{10}$•$10H_2O$. The red line shows the as measured magnetic susceptibility while the blue squares represent corrected data after subtracting a paramagnetic contribution from a small amount of $RuCl_3$ impurity (see text).

3.4 Magnetic Properties of $Li_4Ru_2OCl_{10}$ •$10H_2O$:

The magnetic susceptibility for the compound $Li_4Ru_2OCl_{10}$•$10H_2O$ is presented in **Figure 4**. The compound shows a considerable negative signal and nearly constant magnetic susceptibility at 10 kOe suggesting a diamagnetic behavior in the compound. There is no significant difference in magnetic susceptibility between the zero-field cooling and field cooling measurements at 1 kOe (not shown). However, the increasingly positive magnetic susceptibility at low temperatures is characteristic of a paramagnetic behavior which can be either coming from a paramagnetic impurity or a more complex magnetic behavior from the compound itself. Assuming such a paramagnetic signal is coming from the $RuCl_3$ impurity, it would constitute less than 2% of the total sample mass. In Fig. 4, the corrected magnetic susceptibility after subtracting the paramagnetic impurity contribution is shown by blue squares. It shows a strong temperature-independent diamagnetic behavior, which is reminiscent of the previously reported $[Ru_2OX_{10}]^{4-}$ type compounds (San Filippo *et al.*, 1977; McL Mathieson *et al.*, 1952; Dunitz & Orgel, 1953). The calculated core diamagnetic susceptibility for the $Li_4Ru_2OCl_{10}$ •$10H_2O$ complex is about 4×10^{-4} emu/mol (Bain & Berry, 2008). Comparing with experimental values, the observed strong diamagnetic signal likely

comes from bonded molecular cluster contributions. Structurally, in contrast to the other reported structures with the Ru-O-Ru dimer, the crystal structure of $Li_4Ru_2OCl_{10}$•$10H_2O$ contains two distinct Ru atomic sites generating two types of dimers within the crystal lattice. However, none of the Ru ions bear a clear local magnetic moment based on our magnetization data. This will be further discussed in the following section.

The isothermal magnetic field dependence of magnetization is shown in the SI. The magnetization shows the linear dependence in applied magnetic fields at above 20 K. The negative magnetization observed for these temperatures above 20 K with an applied field further confirms the diamagnetic behavior of the material. Magnetization at 2 K starts with a positive slope, indicating a paramagnetic contribution, and turn to a negative slope at higher field due to its intrinsic diamagnetic behavior. The magnetic isotherms data are consistent with temperature dependent magnetic susceptibility shown in **Figure 4**.

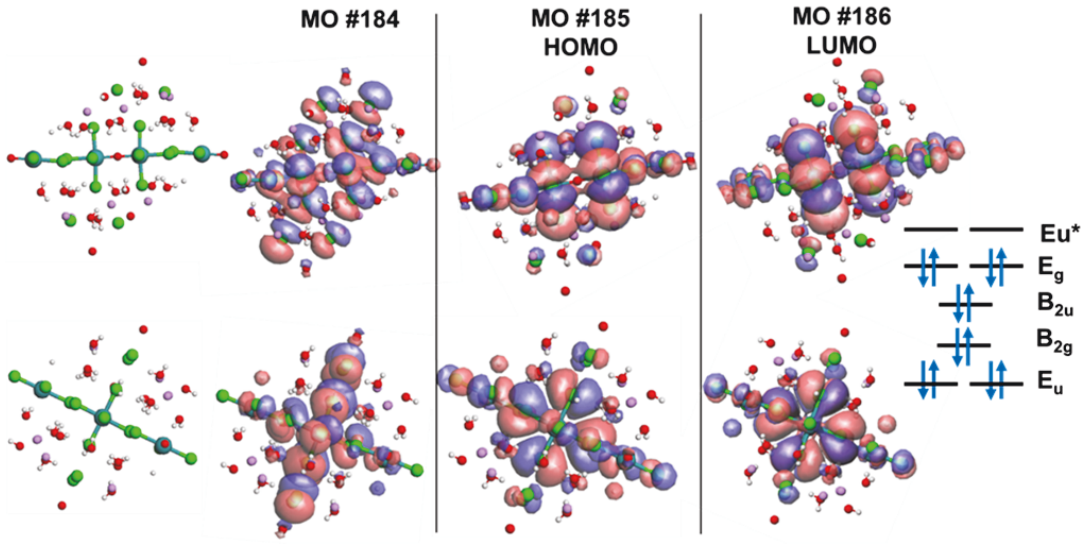

Figure 5

The MO pictures imported from molecular orbital calculations done using CEASER software using the parameters from the single crystal x-ray diffraction results and the qualitative molecular orbital energy level diagram for $Li_4Ru_2OCl_{10}$•$10H_2O$ with the ground-state electron configuration (Total 12 electrons are from two d^4 Ru atoms and filled O p_x and p_y orbitals).

3.5 Molecular Orbital (MO) Diagram of $Li_4Ru_2OCl_{10}$ •$10H_2O$:

To deeply understand and confirm the diamagnetic property of $Li_4[Ru_2OCl_{10}]$ •$10H_2O$, the molecular orbital diagram was generated. According to the results, the energy gap (0.0316 eV) is observed between HOMO (-12.9608 eV) and LUMO (-12.9292 eV), which is consistent with the insulating property of $Li_4[Ru_2OCl_{10}]$•$10H_2O$. Moreover, the *d-p-d* super-interactions dominate the Fermi level in the Ru-O-Ru dimer as indicated in the UV

measurements. The orbital distribution shows (**Figure 5**) there is no unpaired electron on Ru, an indication of a diamagnetic property in agreement with previous studies (Dunitz & Orgel, 1953; Cotton, 1964, 2012).

The bonding arrangement of the dimeric Ruthenium cluster $[Ru_2OCl_{10}]$ can approximately be simplified by idealizing the dimer into a dioctahedral model bridged by the oxygen atom (Cotton, 1964). In each octahedral, the e_g orbitals ($4d_{z2}$, $4d_{x2-y2}$) and $5s$, $5p_x$, $5p_y$, and $5p_z$ orbitals from Ru atoms will interact with the five chlorine and one oxygen σ donor ligands. As a result, six bonding orbitals are formed, filled with donor ligand electrons by forming the octahedral metal-ligand σ bonding framework. The remaining t_{2g} orbitals are involved in the metal-metal bonding bridged by the oxygen. If the symmetry of the $[Ru_2OCl_{10}]$ cluster can be approximately treated as D_{4h} symmetry while the symmetry of each Ru atom will be C_{4v}. Thus, the orbital representations can be approximately marked as $3A_1$, B_1, B_2 and 2E. The chlorine donor ligands would occupy $2A_1$, B_1, and E while the oxygen transforms as A_1 in making the σ bond. For the $[Cl_5\text{-Ru-O-Ru-}Cl_5]^{4-}$ cluster, the symmetry would approximately be treated as D_{4h}. The molecular orbitals arising from the two Ru atoms thus can be represented as B_{2g}, B_{2u}, E_g and E_u from D_{4h} point group. The degenerate Eu orbital from Ru combine with the filled $p_{(x,y)}$ orbital forming a bonding orbital and an antibonding orbital in the Ru-O-Ru system (Dunitz & Orgel, 1953; Cotton, 2012). Accordingly, the molecular orbitals will be in the order of Eu, B_{2g}, B_{2u}, E_g and E_u* with ascending order of energy. The total electrons from two d^4 Ru atoms, filled oxygen p_x and p_y orbitals are 12 which can be resided on the MO diagram as shown in the **Figure 5**.

4 Conclusion

A new ruthenium oxo complex, $Li_4[Ru_2OCl_{10}]$ •$10H_2O$, was synthesized and characterized. $Li_4[Ru_2OCl_{10}]$•$10H_2O$ adopts a different structure from $K_4[Ru_2OCl_{10}]$ •H_2O and $Cs_4[Ru_2OCl_{10}]$ due to the smaller Li^+. The Ru atoms on two distinct sites show the same oxidation state, Ru^{4+}. The diamagnetic properties in $Li_4[Ru_2OCl_{10}]$ •$10H_2O$ indicate no unpaired electron on the Ru atoms in $Li_4[Ru_2OCl_{10}]$ •$10H_2O$. Future studies focus on replacing the neutral water molecule with other anions or cations to tune the oxidation states and magnetic properties on Ru atoms.

Conflicts of interest

There are no conflicts to declare.

Acknowledgement

The work at LSU is supported by NSF-OIA-1832967. We highly appreciate the support given by Dr. Matthew B. Chambers and Dinushini Siddhiaratchi to do the UV-Vis measurements. M.M. was supported by the DOE Office of Science Graduate Student Research (SCGSR) Program and the U.S. Department of Energy, Officeof Science, Basic Energy Sciences, under EPSCoR grant no. DE-SC0012432 with additional support from the Louisiana Board of Regents.

Table 1

Parameters used in the molecular orbital calculation using CAESER software (vers. 2.0, PrimeColor Software, Raleigh, NC, USA) with the extended-Hückel-tight-binding method for $Li_4Ru_2OCl_{10}$•$10H_2O$

Atom	AO	H_{ii} (eV)	ζ_1	c_1	ζ_2	c_2
Ru	**s**	**-10.4000**	**2.0800**	**1.0000**		
	p	**-6.87000**	**2.0400**	**1.0000**		
	d	**-14.9000**	**5.3800**	**0.5340**	**2.3000**	**0.6365**
Cl	**s**	**-26.2999**	**2.1830**	**1.0000**		
	p	**-14.2000**	**1.7330**	**1.0000**		
O	**S**	**-32.2999**	**2.2750**	**1.0000**		
	p	**-14.8000**	**2.2750**	**1.0000**		
Li	**S**	**-5.40000**	**0.6500**	**1.0000**		
	p	**-3.50000**	**0.6500**	**1.0000**		
H	**s**	**-13.6000**	**1.3000**	**1.0000**		

H_{ii} = -VSIP (valence-state ionization potential [eV]). The double-zeta (for Ru 5d) or single-zeta (for the remaining orbitals) Slater type orbitals (STO's) are used;

$\chi_\mu (r, \theta, \phi) \propto r^{(n-1)} \exp(-\zeta r) Y(\theta \phi)$ (single-zeta STO)

$\chi_\mu (r, \theta, \phi) \propto r^{(n-1)} [c_1 \exp(-\zeta_1 r) + c_2 \exp(-\zeta_2 rI)] Y(\theta,\phi)$ (double-zeta STO)

c_1 and c_2 correspond to 1 and 0 in single-zeta STO, and c_1 and c_2 in double-zeta STO, respectively.

Table 2

Single crystal structure refinement data for $Li_4Ru_2OCl_{10}$•$10H_2O$.

Empirical formula	$Li_4Ru_2OCl_{10}$• $10H_2O$
Formula weight (g/mol)	780.56
Temperature (K)	90(2)
Crystal system	Triclinic
Space group; Z	P -1; 2
a (Å)	8.0548(6)
b (Å)	10.7806(8)
c (Å)	13.720(1)
α (°)	78.551(2)
β (°)	80.825(2)
γ (°)	72.163(2)
Volume ($Å^3$)	1105.3(2)
Extinction coefficient	None
Theta range (°)	1.523 to 35.250
No. reflections; R*int*	63759; 0.0244
No. independent reflections	9864
No. parameters	308
R_1: ωR_2 (I>2δ(I))	0.0201: 0.0393
R indices (all data) R_1: ωR_2	0.0269: 0.0416
Goodness-of-fit on F^2	1.106

Table 3

Atomic coordinates and equivalent isotropic displacement parameters of $Li_4Ru_2OCl_{10}$•$10H_2O$ system (U_{eq} is defined as one-third of the trace of the orthogonalized U_{ij} tensor (Å^2)).

Atom	Wyck.	*x*	*y*	*z*	U_{eq}
Ru1	2i	0.37849(2)	0.10506(2)	0.58791(2)	0.00415(2)
Ru2	2i	0.37460(2)	0.58995(2)	0.09582(2)	0.00429(2)
Cl1	2i	0.63765(4)	0.14071(3)	0.62171(2)	0.00776(5)
Cl2	2i	0.33886(4)	0.29470(3)	0.46345(2)	0.00802(5)
Cl3	2i	0.63405(4)	0.61891(3)	0.13762(2)	0.00797(5)
Cl4	2i	0.41256(4)	0.40056(3)	0.21788(2)	0.00836(5)
Cl5	2i	0.10674(4)	0.56616(3)	0.06751(2)	0.00902(5)
Cl6	2i	0.10692(4)	0.08117(3)	0.56365(2)	0.00820(5)
Cl7	2i	0.22222(4)	0.71032(3)	0.22261(2)	0.00873(5)
Cl8	2i	0.60009(4)	0.06856(3)	0.27564(2)	0.00807(5)
Cl9	2i	0.22555(4)	0.24841(3)	0.70076(2)	0.00875(5
Cl10	2i	0.67978(4)	0.20764(3)	0.01953(2)	0.00775(5)
O1	1f	½	0	½	0.0053(2)
O2	1e	½	½	0	0.0057(2)
O3	2i	0.49687(14)	0.05888(10)	0.89617(8)	0.01085(17)
O4	2i	0.17528(13)	0.16393(10)	0.31415(8)	0.01017(17)
O5	2i	0.84841(14)	0.30161(11)	0.18462(8)	0.01244(18)
O6	2i	0.79176(14)	0.24741(10)	0.39722(8)	0.01057(17)
O7	2i	0.26150(16)	0.22692(10)	0.07676(8)	0.01229(18)
O8	2i	0.54028(14)	0.53273(10)	0.39270(8)	0.01096(17)
O9	2i	0.09647(16)	0.02075(10)	0.14455(8)	0.01285(18)
O10	2i	0.10876(14)	0.11580(10)	0.92567(8)	0.01240(18)
O11	2i	0.13884(14)	0.61071(10)	0.46692(8)	0.01124(18)
O12	2i	0.01296(16)	0.44837(12)	0.31953(10)	0.0195(2)
Li1	2i	0.2961(4)	0.0471(4)	0.0217(2)	0.0142(5)
Li2	2i	0.0140(4)	0.2890(4)	0.4167(2)	0.0150(5)
Li3	2i	0.0835(4)	0.1884(4)	0.1848(2)	0.0135(5)
Li4	2i	0.6352(4)	0.3665(4)	0.4937(2)	0.0153(5)

Table 4

Comparison of the structural information of different $A_4Ru_2OCl_{10}$ compounds with the $Li_4Ru_2OCl_{10}$•$10H_2O$.

	$Li_4Ru_2OCl_{10}$• $10H_2O$	$K_4Ru_2OCl_{10}$• H_2O	$Cs_4Ru_2OCl_{10}$	$K_4W_2OCl_{10}$	$Cs_4Os_2OCl_{10}$
Space Group	*P*-1	*I*4/*mmm*	*Pbca*	*I*4/*mmm*	*Pcba*
Lattice parameters /(Å)	a=8.0548(6) b=10.7806(8) c=13.720(1) **α** =78.5510(2) **β** =80.8250(2) **γ** =72.163(2)	a = 7.097(2) c = 17.015(2) **α** =90 **β** =90 **γ** =90	a=12.501(1) b=11.752(1) c=13.923(2) **α** =90 **β** =90 **γ** =90	a = 7.132(2) c = 17.648(5) **α** =90 **β** =90 **γ** =90	a = 12.521 b = 13.994 c = 11.798 **α** =90 **β** =90 **γ** =90
M-O bond length/(Å)	**Ru1:** 1.7838(3) **Ru2:** 1.7808(3)	1.8002(18)	1.7903(12)	1.8710(9)	1.7777(9)
M-O-M bond angle/°	180	180	180	180	180
M-Cl_{ax}/ Å	**Ru1:** 2.3406(4) **Ru2:** 2.3358(4)	2.362(3)Å	2.336(5)	2.407(6)	2.433(7)
M-Cl_{eq}/ Å	**Ru1** 2.3646(5) 2.3633(4) 2.3608(5) 2.3562(4) **Ru2** 2.3489(5) 2.3922(4) 2.3763(5) 2.3431(4)	2.317(8)	2.361(5) 2.365(5) 2.363(5) 2.365(5)	2.4095(16)	2.367(7) 2.371(7) 2.370(6) 2.376(6)
M-Cl*eq* diff/ Å	**Ru1:** 0.008 **Ru2**: 0.05	0	0.004	0	0.009
Equatorial Cl-M-Cl bond angle/°	**Ru1** 90.410(14) 89.352(14) 90.630(14) 89.094(14) **Ru2** 92.054(14) 88.544(14) 89.834(14) 89.222(14)	90	90.35(17) 89.32(17) 89.26(17) 90.36(17)	90	89.0(3) 89.8(3) 89.7(3) 90.6(3)

References

Arii, H., Nagatomo, S., Kitagawa, T., Miwa, T., Jitsukawa, K., Einaga, H. & Masuda, H. (2000). *J. Inorg. Biochem.* **82**, 153–162.

Bai, L.-X., Liu, X., Wang, W.-Z., Liao, D.-Z. & Wang, Q.-L. (2004). *Z. Für Anorg. Allg. Chem.* **630**, 1143–1146.

Bain, G. A. & Berry, J. F. (2008). *J. Chem. Educ.* **85**, 532.

Banerjee, A., Bridges, C. A., Yan, J.-Q., Aczel, A. A., Li, L., Stone, M. B., Granroth, G. E., Lumsden, M. D., Yiu, Y., Knolle, J., Bhattacharjee, S., Kovrizhin, D. L., Moessner, R., Tennant, D. A., Mandrus, D. G. & Nagler, S. E. (2016). *Nat. Mater.* **15**, 733–740.

Barman, S. K., Cano, J., Lloret, F. & Mukherjee, R. (2019). *Inorg. Chem.* **58**, 8086–8099.

Basova, T. V., Kiselev, V. G., Latteyer, F., Peisert, H. & Chassé, T. (2014). *Appl. Surf. Sci.* **322**, 242–248.

Bo, Z., Hu, D., Kong, J., Yan, J. & Cen, K. (2015). *J. Power Sources*. **273**, 530–537.

Boeer, A. B., Barra, A.-L., Chibotaru, L. F., Collison, D., McInnes, E. J. L., Mole, R. A., Simeoni, G. G., Timco, G. A., Ungur, L., Unruh, T. & Winpenny, R. E. P. (2011). *Angew. Chem. Int. Ed.* **50**, 4007–4011.

Butler, K. T., Davies, D. W., Cartwright, H., Isayev, O. & Walsh, A. (2018). *Nature*. **559**, 547–555.

Coey, J. M. D. (2010). Magnetism and Magnetic Materials Cambridge University Press.

Costa, V. V., Jacinto, M. J., Rossi, L. M., Landers, R. & Gusevskaya, E. V. (2011). *J. Catal.* **282**, 209–214.

Cotton, F. A. (1964). *Inorg. Chem.* **3**, 1217–1220.

Cotton, S. A. (2012). Chemistry of Precious Metals Springer Science & Business Media.

Crawford, V. H., Richardson, H. Wayne., Wasson, J. R., Hodgson, D. J. & Hatfield, W. E. (1976). *Inorg. Chem.* **15**, 2107–2110.

Curtarolo, S., Hart, G. L. W., Nardelli, M. B., Mingo, N., Sanvito, S. & Levy, O. (2013). *Nat. Mater.* **12**, 191–201.

Dunitz, J. & Orgel, L. (1953). *J. Chem. Soc. Resumed*. 2594–2596.

Engelmann, X., Monte□Pérez, I. & Ray, K. (2016). *Angew. Chem. Int. Ed.* **55**, 7632–7649.

Fobes, D., Yu, M. H., Zhou, M., Hooper, J., O'Connor, C. J., Rosario, M. & Mao, Z. Q. (2007). *Phys. Rev. B.* **75**, 094429.

Glowiak, T., Sabat, M. & Jezowska-Trzebiatowska, B. 2.

Gorun, S. M. & Lippard, S. J. (1991). *Inorg. Chem.* **30**, 1625–1630.

Grigera, S. A., Borzi, R. A., Mackenzie, A. P., Julian, S. R., Perry, R. S. & Maeno, Y. (2003). *Phys. Rev. B.* **67**, 214427.

Gui, X., Finkelstein, G. J., Graf, D. E., Wei, K., Zhang, D., Baumbach, R. E., Dera, P. & Xie, W. (2019). *Dalton Trans.* **48**, 5327–5334.

Guo, F.-S., Day, B. M., Chen, Y.-C., Tong, M.-L., Mansikkamäki, A. & Layfield, R. A. (2018). *Science*. **362**, 1400–1403.

Halcrow, M. A., Sun, J.-S., Huffman, J. C. & Christou, G. (1995). *Inorg. Chem.* **34**, 4167–4177.

Hoffmann, R. (1963). *J. Chem. Phys.* **39**, 1397–1412.

Huang, Q., Lynn, J. W., Erwin, R. W., Jarupatrakorn, J. & Cava, R. J. (1998). *Phys. Rev. B.* **58**, 8515–8521.

Ikeda, S.-I. & Maeno, Y. (1999). *Phys. B Condens. Matter*. **259–261**, 947–948.

Ishiyama, T. (1969). *Bull. Chem. Soc. Jpn.* **42**, 2071–2074.

Kitaev, A. (2006). *Ann. Phys.* **321**, 2–111.

Kurtz, D. M. (1990). *Chem. Rev.* **90**, 585–606.

Lang, J., Hewer, J. M., Meyer, J., Schuchmann, J., Wüllen, C. van & Niedner-Schatteburg, G. (2018). *Phys. Chem. Chem. Phys.* **20**, 16673–16685.

Li, R., Wang, J., Qi, X.-L. & Zhang, S.-C. (2010). *Nat. Phys.* **6**, 284–288.

Lu, H., Chamorro, J. R., Wan, C. & McQueen, T. M. (2018). *Inorg. Chem.* **57**, 14443–14449.

Maeno, Y., Hashimoto, H., Yoshida, K., Nishizaki, S., Fujita, T., Bednorz, J. G. & Lichtenberg, F. (1994). *Nature*. **372**, 532–534.

Maroń, A. M. & Małecki, J. G. (2014). *Transit. Met. Chem.* **39**, 831–841.

McL Mathieson, A., Mellor, D. P. & Stephenson, N. C. (1952). *Acta Crystallogr.* **5**, 185–186.

Mercier, F., Alliot, C., Bion, L., Thromat, N. & Toulhoat, P. (2006). *J. Electron Spectrosc. Relat. Phenom.* **150**, 21–26.

Morgan, D. J. (2015). *Surf. Interface Anal.* **47**, 1072–1079.

Mousavi, M., Béreau, V., Duhayon, C. & Sutter, J.-P. (2012). *Comptes Rendus Chim.* **15**, 924–928.

Naito, T., Watanabe, N., Sakamoto, Y., Miyaji, Y., Shirahata, T., Misaki, Y., Kitou, S. & Sawa, H. (2019). *Dalton Trans.* **48**, 12858–12866.

Nakatsuji, S., Machida, Y., Maeno, Y., Tayama, T., Sakakibara, T., Duijn, J. van, Balicas, L., Millican, J. N., Macaluso, R. T. & Chan, J. Y. (2006). *Phys. Rev. Lett.* **96**, 087204.

Nguyen, L. T., Halloran, T., Xie, W., Kong, T., Broholm, C. L. & Cava, R. J. (2018). *Phys. Rev. Mater.* **2**, 054414.
Okamoto, Y., Nohara, M., Aruga-Katori, H. & Takagi, H. (2007). *Phys. Rev. Lett.* **99**, 137207.
Overgaard, J., Walsh, J. P. S., Hathwar, V. R., Jørgensen, M. R. V., Hoffman, C., Platts, J. A., Piltz, R. & Winpenny, R. E. P. (2014). *Inorg. Chem.* **53**, 11531–11539.
Perry, R. S., Galvin, L. M., Mackenzie, A. P., Forsythe, D. M., Julian, S. R., Ikeda, S. I. & Maeno, Y. (2000). *Phys. B Condens. Matter*. **284–288**, 1469–1470.
Pesin, D. & Balents, L. (2010). *Nat. Phys.* **6**, 376–381.
Rivero, P., Jin, R., Chen, C., Meunier, V., Plummer, E. W. & Shelton, W. (2017). *Sci. Rep.* **7**, 1–7.
Rollinson, H. & Adetunji, J. (2018). *Encyclopedia of Geochemistry: A Comprehensive Reference Source on the Chemistry of the Earth*, Vol. edited by W.M. White, pp. 738–743. Cham: Springer International Publishing.
San Filippo, J., Fagan, P. J. & Di Salvo, F. J. (1977). *Inorg. Chem.* **16**, 1016–1021.
Sessoli, R., Gatteschi, D., Caneschi, A. & Novak, M. A. (1993). *Nature*. **365**, 141–143.
Sharninghausen, L. S., Sinha, S. B., Shopov, D. Y., Choi, B., Mercado, B. Q., Roy, X., Balcells, D., Brudvig, G. W. & Crabtree, R. H. (2016). *J. Am. Chem. Soc.* **138**, 15917–15926.
Sheldrick, G. M. (2015). *Acta Crystallogr. Sect. C Struct. Chem.* **71**, 3–8.
Silva, R. S. da, Zukerman-Schpector, J., Tfouni, E. & Lever, A. (1999). *Z. Krist.-New Cryst. Struct.* **214**, 303–304.
Singh, M. K. & Rajaraman, G. (2019). *Inorg. Chem.* **58**, 3175–3188.
Steffens, P., Farrell, J., Price, S., Mackenzie, A. P., Sidis, Y., Schmalzl, K. & Braden, M. (2009). *Phys. Rev. B*. **79**, 054422.
Stone, M. B., Lumsden, M. D., Jin, R., Sales, B. C., Mandrus, D., Nagler, S. E. & Qiu, Y. (2006). *Phys. Rev. B*. **73**, 174426.
Tebbe, K.-F. & Schnering, H. G. V. (1973). *J. Inorg. Gen. Chem.* **396**, 66–80.
Walsh, J. P. S., Sproules, S., Chilton, N. F., Barra, A.-L., Timco, G. A., Collison, D., McInnes, E. J. L. & Winpenny, R. E. P. (2014). *Inorg. Chem.* **53**, 8464–8472.
Zhou, Y., Kanoda, K. & Ng, T.-K. (2017). *Rev. Mod. Phys.* **89**, 025003.
Zhuo, Y., Mansouri Tehrani, A. & Brgoch, J. (2018). *J. Phys. Chem. Lett.* **9**, 1668–1673.
Zimmermann, T. P., Limpke, T., Stammler, A., Bögge, H., Walleck, S. & Glaser, T. (2018). *Inorg. Chem.* **57**, 5400–5405.